An Inkjet-Printed Microfluidic RFID-Enabled Platform for Wireless Lab-on-Chip Applications

Benjamin S. Cook, *Student Member, IEEE*, James R. Cooper, *Student Member, IEEE*, and Manos M. Tentzeris, *Fellow, IEEE*

***Abstract*—This paper introduces the first-of-its-kind wireless passive sensing platform combining radio frequency identification (RFID), microfluidics, and inkjet printing technology that enables remote fluid analysis and requires as little as 3 μL of fluid. The demonstrated variable microfluidic capacitors, resonators, and RFID tags are fabricated using a novel rapid, low-cost, and low-temperature additive inkjet process, making them disposable. However, even with their disposable nature, the RF microfluidic devices exhibit repeatability and long-term reusability for accurately detecting water, various alcohols, and % content of water/alcohol mixtures down to 1% water in ethanol. While the main discussion is on fluid sensing, the demonstrated components can also be used in fluid-tunable RF applications.**

***Index Terms*—Antennas, inkjet printing, microfluidics, passive sensors, radio frequency identification (RFID), wireless sensors.**

I. Introduction

MICROFLUIDICS have become a valuable tool over the past decade to manipulate, analyze, and interact with tiny amounts of liquid in applications ranging from blood analysis, bio-assays, and manufacturing quality control. Before microfluidics, processes such as bio-assays and water-quality analysis required large amounts of liquid ranging from milliliters to several liters, the majority of which is wasted in dead volume required to fill tubing and valves and never utilized for analysis or measurement purposes. However, with the introduction of microfluidic systems, fluid analysis can be performed on samples of the order of microliters due to the monolithic integration of sensing and interface electronics, fluidic manipulation structures, and micrometer-sized fluid channels on a single packaged chip.

Microfluidic devices are typically fabricated utilizing cleanroom processing as standard lithographic processes lend well to producing micrometer-sized encapsulated fluid channels as well as the required interface electronics. These processes, however, are time-consuming, costly, and require the use of harsh chemicals. Because of these issues, extensive research has gone into alternate fabrication methods that allow for simple, low-cost, and rapid production of microfluidic devices. Several methods, such as laser-etched fluidics, craft cut fluidics, and wax-impregnated capillary action fluidics on paper, have emerged that can be produced outside of a cleanroom environment in a simple manner [1]–[3]. However, one of the obstacles with current low-cost microfluidics is integrating electronics while keeping the devices low cost, as patterning interface and sensing microelectronics onto the chip still requires the use of standard cleanroom processes.

In this paper, a novel approach is proposed that allows for the fabrication and monolithic integration of low-cost microfluidic channels with RF interface microelectronics by utilizing multilayer inkjet printing fabrication techniques. Inkjet printing is a rapid and additive process that can deposit a wide variety of materials, including metals, dielectrics, and nanomaterial-based sensors, at a low cost and with negligible material waste [4]–[8]. Utilizing a layer-by-layer inkjet deposition technique that has previously been characterized in [4], [5], interface electronics and printed adhesive layers are deposited onto a base substrate that can be bonded with laser-etched fluid channels to produce fully integrated RF microfluidic sensing systems [9]. The inkjet fabrication process is utilized in this work to demonstrate tunable microfluidic RF capacitors, resonators, and the first-ever wireless passive laboratory on chip. The proposed "zero power" inkjet-printed microfluidic sensing platform can be targeted towards large-scale distributed water-quality measurement, process monitoring, and biomedical analysis due to its low-cost nature.

TABLE I
Electrical Parameters at 900 MHz and 300 K [10], [11]

Fluid	Re(Permittivity) ϵ'	Im(Permittivity) ϵ''
Water	73	5
Ethanol	15	11
Hexanol	3	2.5

II. Theory of Operation

At microwave frequencies, fluids exhibit large differences in their electrical parameters, such as permittivity (ϵ_r), conductivity (σ), and loss $(\tan\delta)$, some of which are displayed in Table I. Due to the large variability in the constitutive parameters of different fluids at high frequency, the introduction of different fluids into a microwave system can cause drastic changes in the system properties based on field interactions with the fluid.

Manuscript received June 17, 2013; revised September 03, 2013, September 10, 2013; accepted September 30, 2013. Date of publication November 20, 2013; date of current version December 02, 2013. This work was supported in part by the National Science Foundation and the NEDO Foundation. This paper is an expanded paper from the IEEE International Microwave Symposium, Seattle, WA., USA, June 2–7, 2013.

The authors are with the School of Electrical and Computer Engineering, Georgia Institute of Technology, Atlanta, GA 30332 USA (e-mail: benjamin.cook@gatech.edu).

Color versions of one or more of the figures in this paper are available online at http://ieeexplore.ieee.org.

Digital Object Identifier 10.1109/TMTT.2013.2287478

This idea has recently led to the introduction of fluid-tunable microwave systems, and the similar reciprocal fluid sensing utilizing microwave systems. The majority of the current fluid-integrated microwave systems in the literature utilize the fluid as a replaceable dielectric for transmission lines, microwave resonators, or antennas [12]–[21]. By introducing fluids with different constitutive parameters as the dielectric, the propagation constant on transmission lines, or the resonance of a resonator or antenna can be changed. However, the majority of these systems utilize complex fabrication techniques, or utilize large-scale fluidics.

In this paper, we demonstrate tunable microfluidic resonators and antennas that operate based on a microfluidic loaded capacitive gap that acts as the tuning mechanism. The capacitive gap is an area of high electric-field concentration. As the field concentration is high in this region, introducing very small amounts of fluids allows for large changes in the impedance of the gap. These changes are dependent on the constitutive parameters of the fluid or a mixture of fluids that flow through the gap, which makes the gap a fluid-dependent varactor. This fluid-dependent varactor can then be used to load microwave resonators and antennas to tune their frequency of operation.

III. Fabrication

The materials used are 1/16-in-thick cast acrylic sheets (Poly(methyl-methacrylate)) (PMMA) (Mcmaster-Carr, Atlanta, GA, USA) into which the microfluidic cavities and channels are etched, 220-μm-thick Kodak Premium Photo Paper, which is used as the bonding substrate (Office Depot), Cabot CCI-300 suspended, silver nanoparticle ink (Cabot Corporation, Boston, MA, USA) for printing out the conductive features; an SU-8 polymer solution (MicroChem, Newton, MA, USA) for use in bonding the PMMA and the paper substrate, and for sealing the paper substrate from direct contact with the fluid-under-test, and Circuit Works 60 Minute Cure Conductive Epoxy (Chemtronix, Kennesaw, GA, USA) for attaching RF connectors and RFID chips. The process for constructing the varactors, and all structures that utilize the varactor, is as follows. The PMMA sheets are etched, using a laser etching machine, with channels and cavities for storing and moving the fluid-under-test. The patterned metallization is inkjet printed onto the photo paper using a Dimatix DMP-2800 Inkjet Printer and cured in an oven under standard atmosphere. The photo paper and PMMA sheets are then bonded together using an inkjet patterned SU-8 bonding layer. During bonding, the bonding agent is cured on a hotplate. A diagram of this process can be seen in Fig. 1.

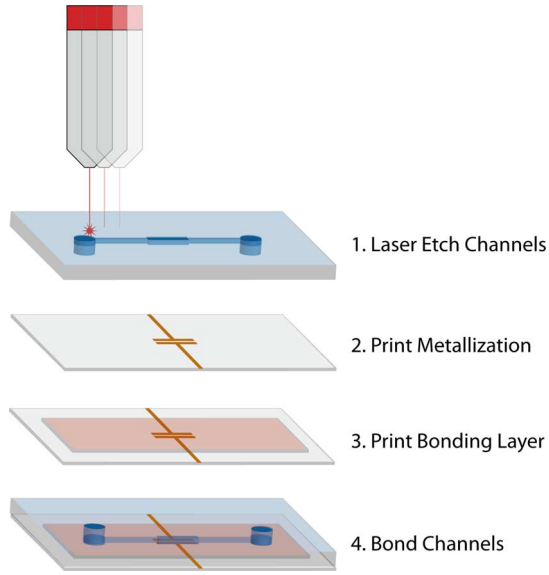

Fig. 1. Inkjet microfluidics process overview.

A. Etching of Cavities and Channels

The fluid inlet/outlets, which allow a fluid-under-test to pass into and out of the system, the microfluidic cavities, which hold the fluid-under-test atop the varactors, and the microfluidic channels, which transport the fluid-under-test between the cavities and the fluid inlets/outlets, are etched in a 1.5-mm-thick PMMA sheet via laser etching. The etching is performed using an Epilog Mini 24 etching system utilizing a 650-nm wavelength 40-W laser. The laser runs under two modes, raster and vector. Raster mode is used to create the cavities, as it allows for large-area engraving, and vector mode is used to etch the channels and to cut out the fluid inlets/outlets as it allows for finer features. Etching is performed with the PMMA at the focal point of the laser when fine features and sharp edges are desired and run with the PMMA 5 mm below the focal point of the laser when smooth features and rounded edges are desired.

Parametric sweeps are run in order to create an etching profile for the cavities and channels. First, a sweep is done in the raster mode for the cavities, where the power is swept from 15% to 45%, in increments of 5%, while the laser is in focus and again while out of focus. The speed is kept constant at 10% maximum speed for the laser, and the laser pulsing frequency is kept constant at 5 kHz. The extracted depths of the cavity etches for different power levels, in focus and out of focus, can be seen in Fig. 2(a) and (b), respectively. Cross-sectional profiles of the cavity etches created by the parametric sweep, for both in focus and out of focus, can be seen in Fig. 3. The width of the cavity etches remains nearly constant under the different power levels, at 1.04 mm for in-focus etching and 1.12 mm for out-of-focus etching. In order to make the cavities such that they contain less than 25 μL or about half a drop of water, a power level setting of 14 W, while the laser is out of focus, was chosen.

Following cavity etching, a sweep is done in the vector mode to determine the etching profile for the channels, where power is swept from 3% to 11% in increments of 2%, while in and out of focus. The speed is kept constant at 7% of maximum speed for the laser, and the laser pulsing frequency is kept constant at 5 kHz. The extracted depths of the channel etches at different power levels, in focus and out of focus, can be seen in Fig. 2. Cross-sectional profiles of the channel etches under the sweep, for both in focus and out of focus, can be seen in Fig. 3. The width of the channels under the in-focus sweep remains constant under variation in power, at 100 μm. The widths of the channels when the PMMA is 5 mm below the focal point vary depending on the power level from 250 to 375 μm. The sharp edges of the in-focus channel etchings can exacerbate microfracturing which occurs during heating of the PMMA. Also, the narrow profile

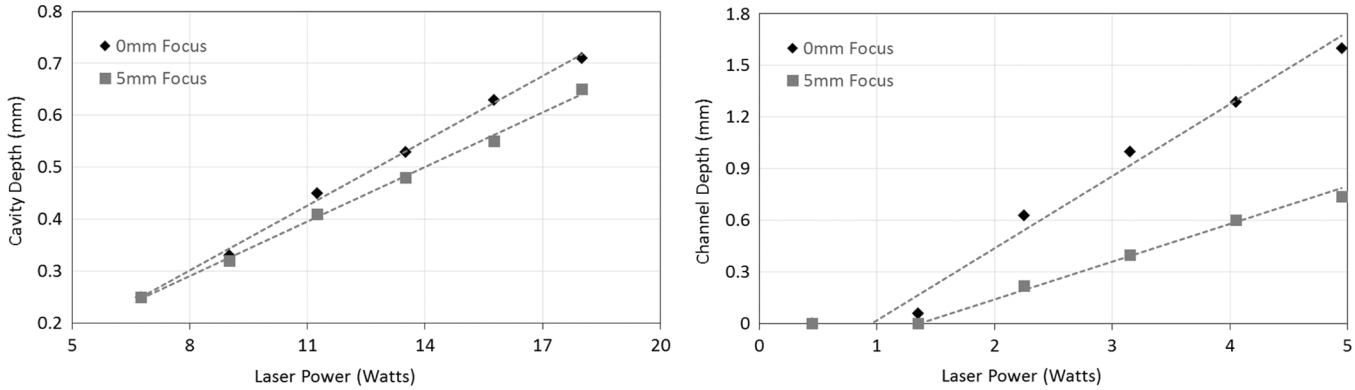

Fig. 2. (a) Channel depth versus laser power for in- and out-of-focus settings. (b) Cavity depth versus laser power for in- and out-of-focus settings.

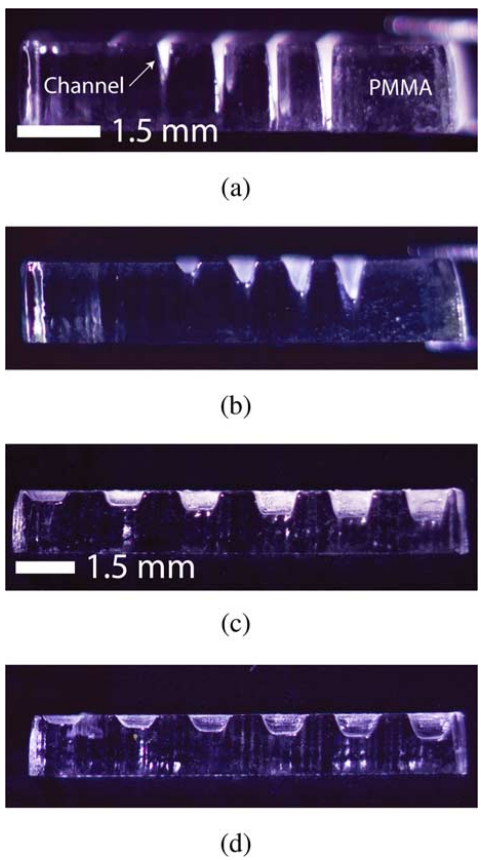

Fig. 3. (a) In-focus vector cut channels. (b) The 5-mm out-of-focus vector cut channels. (c) In-focus raster cut cavities. (d) The 5-mm out-of-focus raster cut channels.

of the in-focus etching can make the channels more susceptible to clogging by the SU8 applied in the bonding phase. Therefore, an out-of-focus etching profile is used for the rest of this work. A power level of 2.25 W was chosen for the etching of the channels on the varactor in order to guarantee easy flow of the fluid-under-test as well as minimizing the total fluid volume in the channels to submicroliter volumes.

The laser etcher is also used to cut out the final microfluidic chip. This includes the fluid inlets/outlets for connecting feed tubing, and any cutout which might be necessary for placing RF connectors or surface mount devices. This was done using 8 W at a 7% speed while the laser is in focus.

B. Dimatix Printing Platform

The printing platform used is the Dimatix DMP-2831 materials deposition printer. The print heads for the Dimatix are designed to work with a viscosity in the range of 8 to 12 cP, and a surface tension in the range of 20–30 mN/m. The minimum feature size obtainable by this printing platform is approximately 20 μm [4].

C. Printing of Metallization Layer

The Cabot CCI-300 ink consists of silver nanoparticles suspended in an organic solvent mixture. It has a viscosity of 12 cP, which has been tuned such that it is printable in standard drop-on-demand (DOD) piezoelectric-based printer heads. The conductive traces are printed onto Kodak paper using a drop spacing of 20 μm, a print head temperature of 35 °C, a printer platen temperature of 45 °C, and a jetting frequency of 5 kHz. Three layers of the silver ink are printed in order to obtain a high-conductivity metallization layer [4], [22]. The photo paper, with printed traces, is raised to 120 °C in a Thermo Scientific oven. It is kept at that temperature for 30 min, until the solvent in the ink is completely dissolved. The metallized substrates are then flash cured at 180 °C for 5 min in order to fuse the silver nanoparticles together and yield a metal conductivity of 1.1e7 S/m. A flash curing is necessary due to paper having a low burning temperature.

D. Printing of Bonding Layer

After etching the channels and cavities and printing the conductive traces, the PMMA sheets and photo paper are aligned and bonded together to seal the microfluidic channels. For bonding the PMMA layer to the photo paper, an SU-8 ink that is tuned for the Dimatix platform [5] is patterned where the channels will contact the paper substrate as to minimize material usage. To ensure no fluid leakage occurs, an extra 5 mm of SU-8 is printed around any critical points in order to ensure a tight seal. The thickness of three SU-8 layers printed on the Kodak paper is approximately 15 μm [5]. The total thickness of the bonding layer is chosen such that there is sufficient SU-8 to ensure a perfect seal around the cavities, channels, and fluid

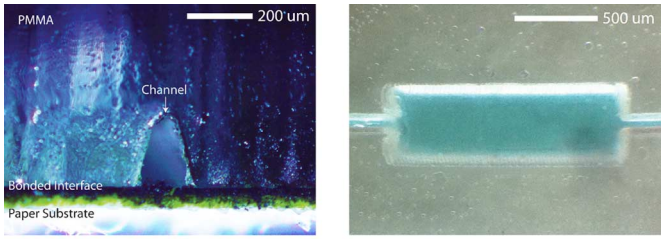

(a) (b)

Fig. 4. (a) Laser-cut cross section of PMMA with etched channel bonded to paper substrate. (b) Top-down view of a PMMA-etched microfluidic cavity bonded onto paper filled with fluid.

inlets/outlets and to form a tight bond between the PMMA and paper substrate. Too much SU-8 can cause excess solution to flow into and clog the channels during bonding. A thicker SU-8 layer also leads to a decrease in the coupling between the printed traces and the fluid-under-test, thus leading to lower sensitivity in the measurements.

E. Bonding and Curing

For bonding the PMMA to the paper substrate, after printing the SU8, the paper substrate is placed in a low energy UV oven in order to activate the SU-8 crosslinker. A total exposure of 100 mJ/mm^2 at 365 nm is used. Once the crosslinker is activated, the PMMA and paper substrate are bonded at a constant pressure of 10.5 N/cm^2 while the structure is slowly raised to 100 °C to complete the bonding. The continued pressure serves to keep the two surfaces in contact to prevent the PMMA from warping and to remove any air bubbles that may degrade the integrity of the bond. A cross-sectional view of a channel after the bonding process can be seen in Fig. 4, along with a top-down view of the channel filled with liquid. From the image, it can be seen that very little of the SU-8 is sucked into the channels, thereby not altering the volume and cross-sectional areas present in Section III-A.

F. Post Bonding Processing

After bonding, a tubing is connected to the fluid inlets/outlets in order to move fluid into and out of the measurement system. The tubing is secured to the fluid inlets/outlets using a super glue, which partially melts the PMMA and forms a solid seal. Any RF connectors or surface mount components are attached to the metallization using conductive epoxy. The epoxy is cured in an oven at 80 °C for 20 min in order to avoid warping of the PMMA.

G. Stability and Fluid Compatibility

The fluid compatibility of the bonded microfluidic channels is dependent on the two materials that construct the channel—etched PMMA and an SU-8 seal. After curing, SU-8 has a very high chemical resistance. PMMA is resistant to most polar solvent, but is not compatible with most nonpolar solvents.

The temperature stability of the microfluidic devices is limited by the glass transition temperature of the PMMA which is 105 °C.

IV. Microfluidic Varactor

The fundamental building block of the tunable microwave resonators and antennas in this work is the microfluidic varactor shown in Fig. 5. The varactor consists of a planar capacitive structure with a 500-μm gap that is fed using microstrip feed lines. A 500-μm deep fluid cavity etched in PMMA is bonded directly over the gap to allow for delivery of the fluid. The entire device is fabricated using the process outlined in Section III.

To simplify the simulation of tunable devices in the following sections that utilize the microfluidic varactor as a fundamental building block, the ability to model the varactor as a lumped element in the system would be ideal and greatly decrease simulation time. The electrical properties of the materials are $\epsilon_{r(\text{paper})} = 3.1$, and $\tan_{\delta(\text{paper})} = 0.06$ [4], $\epsilon_{r(\text{SU8})} = 3.0$, and $\tan_{\delta(\text{SU8})} = 0.04$ [23], and $\epsilon_{r(\text{PMMA})} = 3.5$, and $\tan_{\delta(\text{PMMA})} = 0.04$ [24]. In order to create the lumped model, TRL calibration structures are fabricated to de-embed the microstrip feeds, and the S-parameters of the gap are measured from 0 to 8 GHz using a Rhode and Schwartz ZVA-8 vector network analyzer (VNA). The varactor is loaded with ethanol, hexanol, water, and various combinations of the three to produce a fluid and frequency-dependent model. The net permittivity of the mixtures is determined by the Looyenga formula, which assumes linear mixing and no chemical reactions [25].

De-embedding of the connectors and feed lines is performed using WinCal to move the reference plane up to the outer edge of the capacitive pads. The series capacitance of the gap is then extracted directly from the de-embedded S-parameters. Fig. 6 displays the frequency-dependent capacitance and quality factor of the varactor for various fluids in the cavity. When fluid is introduced, it is noticed that the capacitance decreases over frequency. This is due to the high dispersion present in the fluids used in this study, which exhibit a large decrease in permittivity near 1 GHz [10], [11]. The capacitance when the fluid cavity is empty is approximately 0.05 pF and is stable until the self-resonant frequency (SRF) is reached near 7 GHz. Introducing 1-hexanol, ethanol, and water, which each have increasingly higher permittivities, incrementally increase the capacitance of the gap from 0.05 to 1.25 pF at 900 MHz, which is approximately a 2500% increase. The large changes in capacitance will allow for wide tuning ranges in microwave components and sensors, which are demonstrated in the following sections. However, the SRF decreases from 7 GHz to approximately 4 GHz as the capacitance increases, meaning that tunable components must be operated under 4 GHz to avoid the unwanted effects of utilizing the gap above its SRF.

To test the sensitivity of the gap, a study is performed in which varying amounts of water are added to a 100% ethanol solution in 1, 3, 10, and 25 w% concentrations. Very distinct capacitance increases can be seen with even 1% by weight additions of water in ethanol, which can be attributed to the net increase in permittivity of the solution. For 1 w% water in ethanol, the impedance changes nearly 4%, and for 3 w% water in ethanol, the impedance changes 8.2% at 900 MHz. While these changes may seem small for standard R-C rise time measurements, they are not trivial when used for tuning of microwave components,

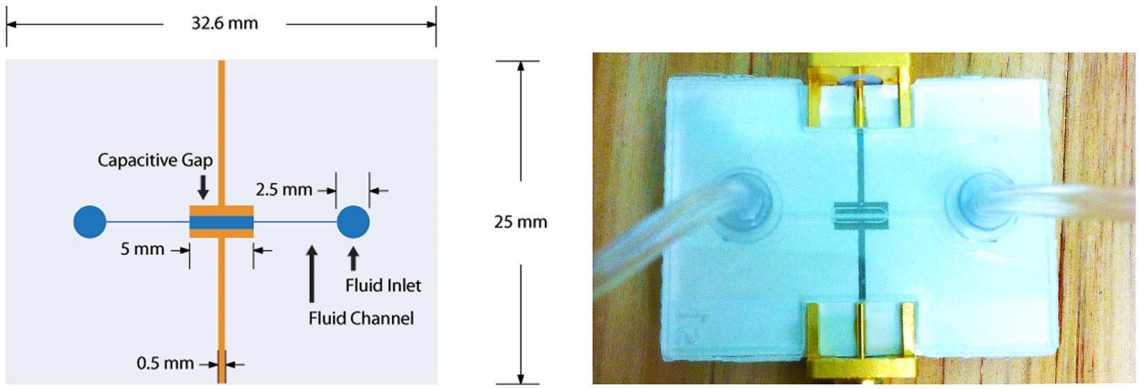

Fig. 5. (a) Scale-drawn schematic of fabricated microfluidic varactor. (b) Fabricated microfluidic varactor with mounted SMA connectors for performing microwave capacitance measurements.

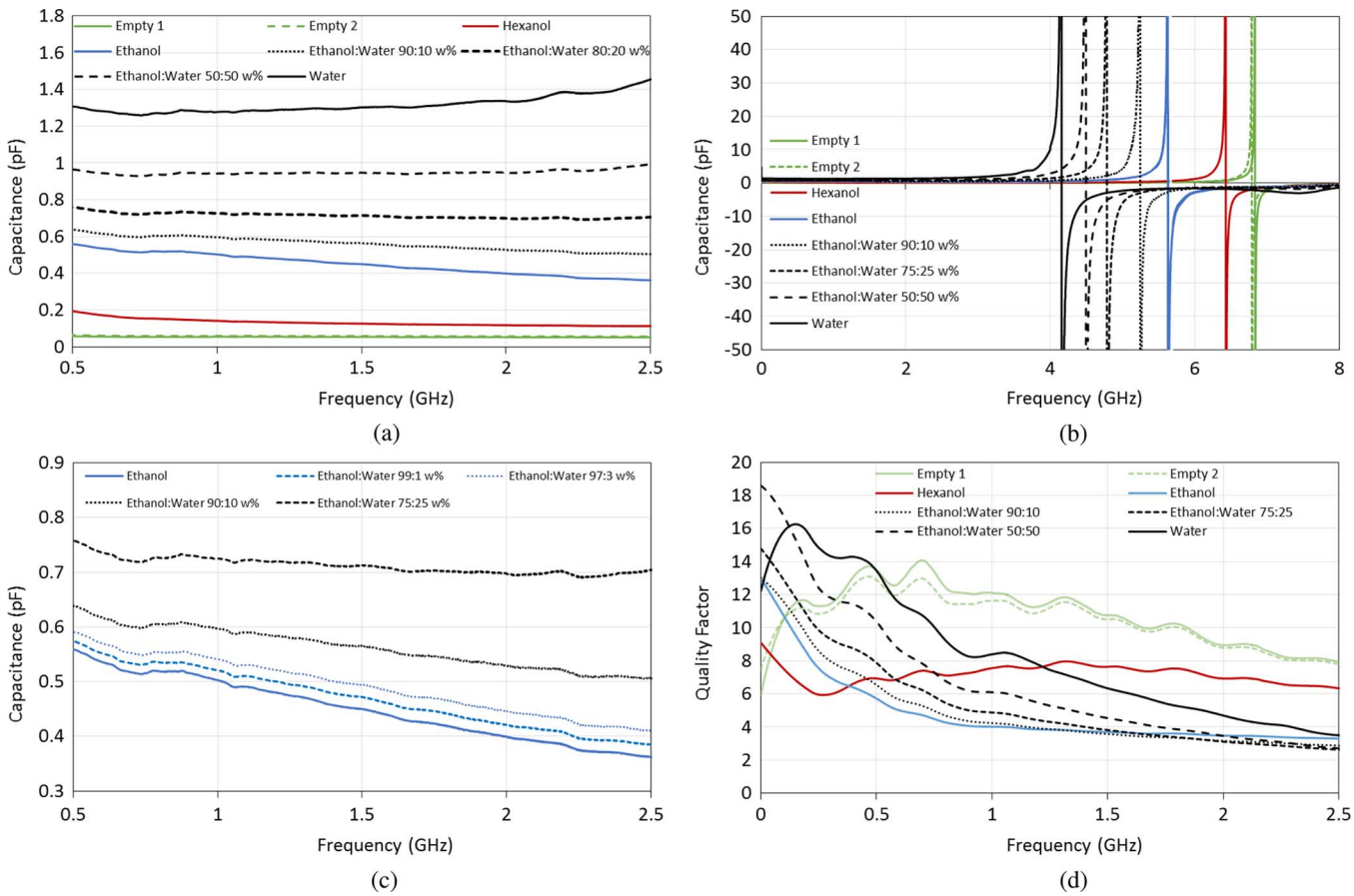

Fig. 6. (a) De-embedded frequency-dependent capacitance of the microfluidic varactor for different fluids. (b) De-embedded self-resonant frequency of the microfluidic varactor for different fluids. (c) De-embedded capacitance of the microfluidic varactor for various concentrations of water in ethanol. (d) Measured varactor quality factor.

as small impedance changes can translate into large resonant frequency shifts.

The capacitance at 900 MHz versus the net permittivity of the solution is compared with simulation in Fig. 7. A very good agreement is obtained in both the capacitance value and trend as the fluid permittivity increases, and as fluids are mixed. The high sensitivity in capacitance of 17.5 pF/ϵ_r and linearity versus permittivity demonstrated by the varactor lends itself well to tuning and sensing applications. State-of-the-art works show capacitance sensitivities of approximately 12 pF/ϵ_r [26], [27].

V. Microfluidic Resonator

Varactors are a common component used in the tuning of microwave devices, such as resonant tanks, filters, and voltage controlled oscillators. In this section, the varactor demonstrated

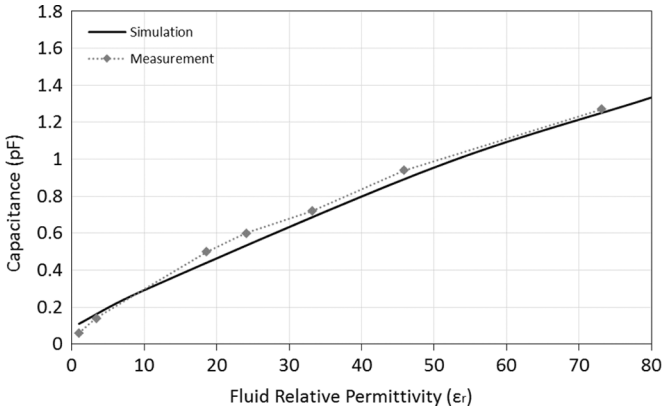

Fig. 7. Measured and simulated linearity of the varactor.

previously is used to tune the resonant frequency of a microstrip T-resonator by changing its electrical length.

The microstrip T-resonator used in this work is shown in Fig. 8. The resonator is designed for a 2.4-GHz center frequency of operation to keep the size small and to demonstrate that the varactor model created in Section IV is valid through the 2.4-GHz band. The microstrip T-resonator is a length of transmission line with an open-circuit stub. The resonator has a null in the insertion loss when the reflected wave from the stub is 180° out of phase or when the length of the open-circuit stub is approximately $(\lambda)/(4)$. The equation for resonance is shown in

$$f_r = \frac{nc}{4(L + L_0)\sqrt{\epsilon_{\text{eff}}}} \tag{1}$$

where n is the resonance mode, i.e., $(n = 1, 3, 5, \ldots)$, c is the speed of light in free space, L is the length of the open-circuit stub, L_0 is the correction factor for the fringing capacitance at the end of the stub, and ϵ_{eff} is the effective permittivity of the microstrip line [28].

By inserting the varactor in series with the open circuit stub, the effective length of the stub is changed upon introduction of different fluids. With no fluid in the gap, the capacitance is 0.05 pF or $-j8 \times 10^3\,\Omega$, which is essentially an open circuit at 2.4 GHz. However, when water flows through the gap, the capacitance increases to 1.5 pF, or $-j2.5 \times 10^2\,\Omega$, at 2.4 GHz; the impedance decreases, making the varactor appear closer to an RF short than an RF open. As the reactance of the gap decreases, the effective length of the open-circuit stub increases, which effectively decreases the resonant frequency of the resonator.

The T-resonator is constructed as in Fig. 8. For simulation, a discrete impedance model is used to replace the gap which helps reduce the simulation time. The series gap impedance for each fluid is extracted from the de-embedded capacitive gap in the previous section for use in the simulation.

Fig. 9(a) displays the measured insertion loss of the resonator for various fluids. With an empty cavity, there is a resonance at 2.4 GHz. By introducing the various fluids used previously for the varactor, the resonator is tuned down to 1.8 GHz. The sensitivity in resonant frequency is approximately $0.35\%/\epsilon_r$. This is comparable to the tunability of state-of-the art fluid-based resonators and frequency-selective surfaces which achieve sensitivities of $0.25\%/\epsilon_r$ [17] and $0.05\%/\epsilon_r$ [21], respectively. The quality factor is lower with fluids such as ethanol as the dielectric loss is high, however, this can be easily improved by utilizing different fluids, as can be seen with deionized water.

VI. Passive Wireless Laboratory-on-Chip

Moving away from wired microwave components, an area of potential high impact that can be enabled by the fluid varactor is wireless microfluidic-based laboratory-on-chip (LOC). Wireless LOC systems allow for the remote analysis of fluids in biomedical, production and potentially hazardous environments where wired measurements are not feasible or cost-effective. Currently, however, wireless LOC systems require a power source that increases cost and decreases life span.

By utilizing the microfluidic varactor to tune an RFID antenna utilizing a similar method to the T-resonator, a completely passive RFID-based LOC platform is demonstrated for the first time. The design for the microfluidic RFID antenna is shown in Fig. 10, which consists of a meandered dipole antenna, fluid varactors to change the electrical length of the antenna and a T-matching network for the RFID chip which will be used for communication. The microfluidic RFID antenna is designed to match the impedance of the Alien Technologies Higgs 3 EPC Gen-2 RFID chip, which is approximately $16+\text{j}200\,\Omega$. As the readable range of the Voyantic Tagformance reader is 800–1000 MHz, the antenna is designed to resonate near 1000 MHz when empty so that the downward shifts caused by the introduction of fluid can be captured. The design is optimized for these parameters using the CST frequency domain solver. The same gap model extracted from Section IV is utilized to simulate the expected resonant shifts in the antenna.

To confirm the agreement of the fabricated tag with the simulation before wireless backscatter measurements are performed, a cabled measurement of the return loss of the antenna is performed using a Rhode and Schwartz ZVA-8 VNA. The measured S-parameters are then re-normalized to the RFID chip impedance, as displayed in Fig. 11(a). The return loss shows matching at 1 GHz when the channel is empty, which is confirmed in simulation. The various fluids utilized in the previous sections are then pumped through the fluidic channels while the return loss is measured. Distinct downward shifts in the resonance confirm that the fluidic channel is loading the capacitive gap on the antenna and increasing the electrical length. Large shifts of nearly 100 MHz are achieved in the cabled measurement. The shifts experienced in the cabled measurement are compared with simulation utilizing the gap model in Fig. 11(b), and the best fit curves show a difference below 6%.

Following cabled verification of the passive microfluidic tag, the Alien RFID chip is mounted on the tag, and a wireless measurement setup is constructed as displayed in Fig. 12. The tag is placed 0.5 m away from the reader antenna of the Tagformance, which interrogates the tag across the 800–1000-MHz band. The interrogation distance was fixed by the setup available in the anechoic chamber. The Tagformance returns data on power required to activate the tag and the reflected power and phase versus frequency. A single frequency sweep takes approximately 10 s. This can be decreased by lowering the frequency resolution. Again, the tag is measured with an empty

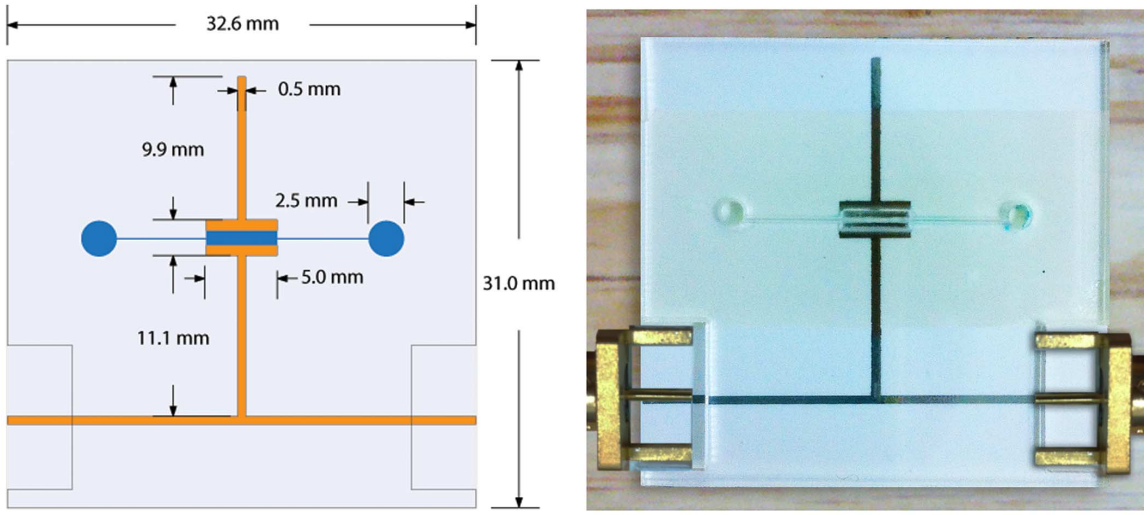

Fig. 8. (a) Scale-drawn schematic of the fabricated microstrip T-resonator with embedded varactor. (b) Fabricated microfluidic tunable microstrip T-resonator.

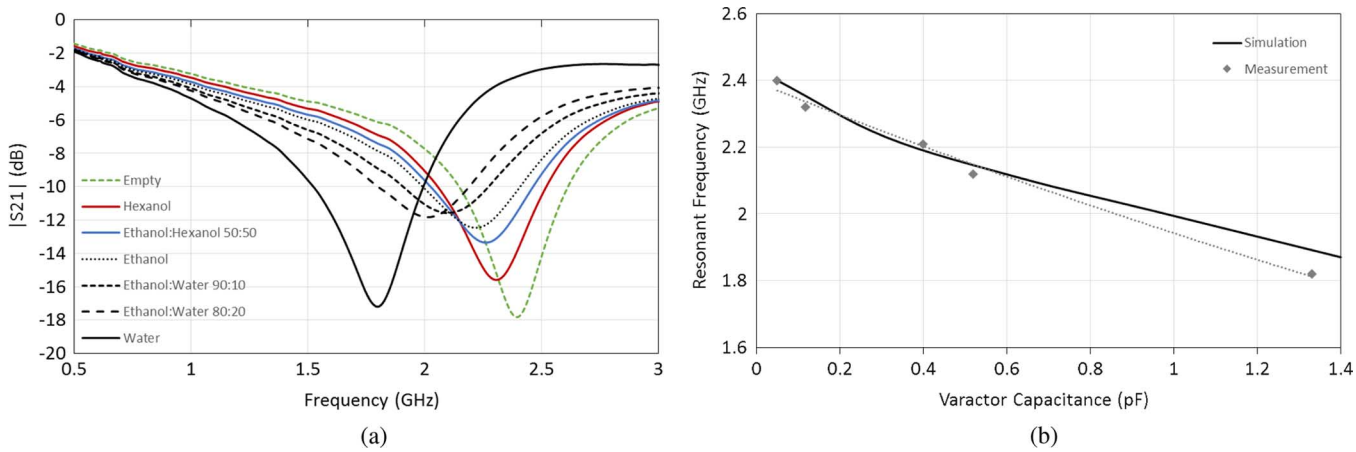

Fig. 9. (a) Insertion loss of the microfluidic T-resonator with different fluids. (b) Simulated and measured response of the T-resonator using the discrete capacitance model of the microfluidic varactor.

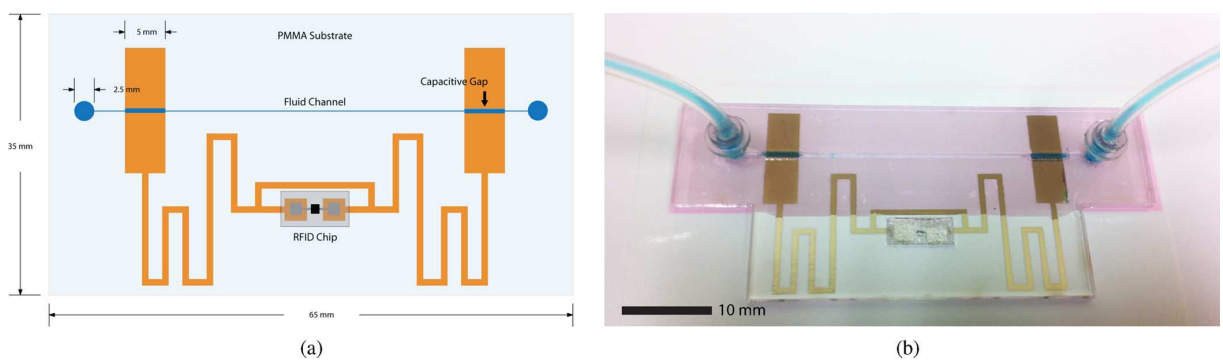

Fig. 10. (a) Scale-drawn RFID-based microfluidic sensor. (b) Fabricated RFID-based microfluidic sensor demonstrating fluid flow.

channel and all of the fluids used in the cabled measurement. The data returned from the Tagformance, which is shown in Fig. 11(c), displays the transmit power required to activate the tag versus frequency along with the second-order curve fit in MATLAB, which is used to extract the resonant frequency. A clear downward shift in the resonant frequency is experienced as higher permittivity fluids are sent through the channel as is expected, and the resonant shift versus fluid permittivity is plotted in Fig. 11(b), against simulation and cabled measurement. After all of the liquid measurements are performed, the

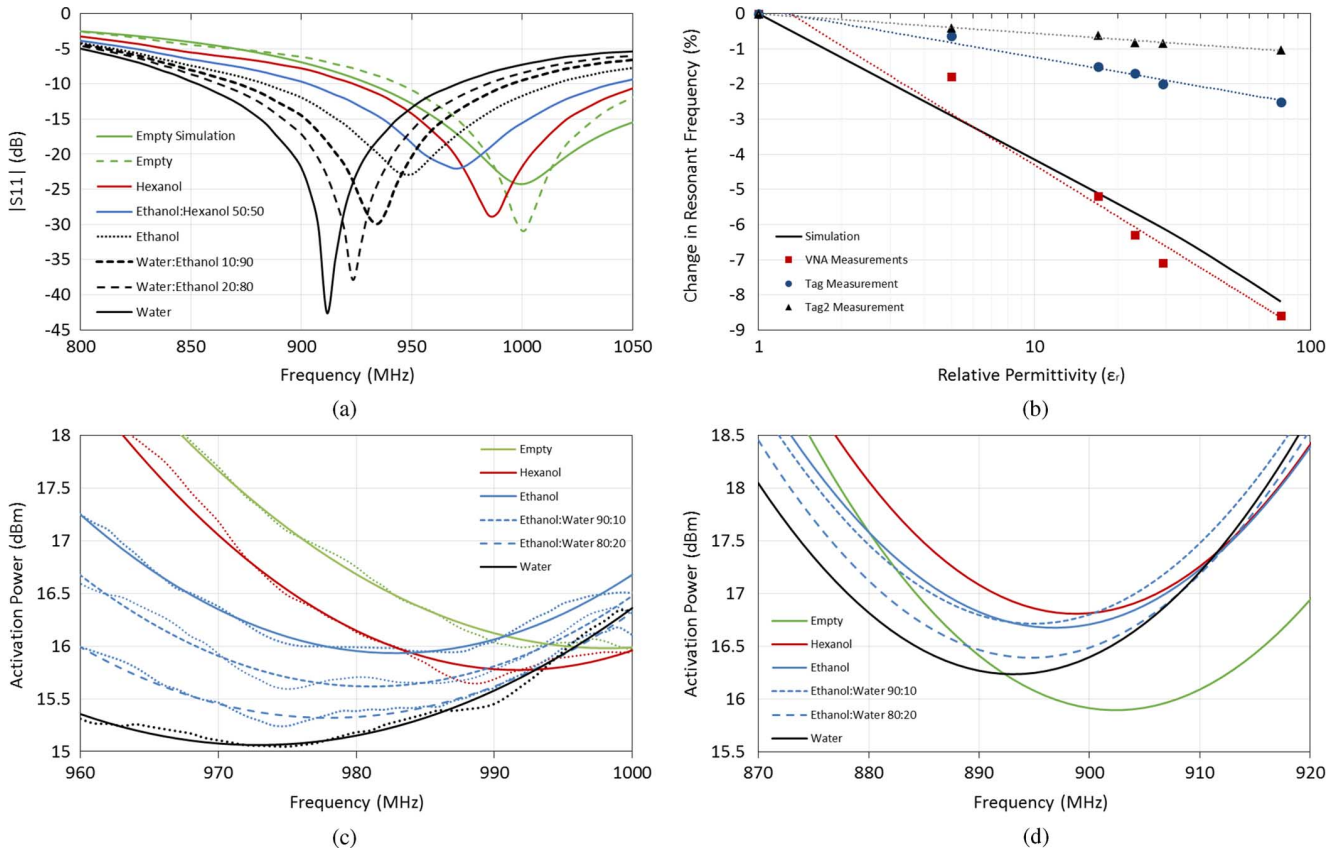

Fig. 11. (a) Measured S-parameters of the microfluidic RFID tag. (b) Comparison of simulated and measured return loss of the microfluidic RFID antenna, along with wireless chip measurements. (c) Curve fit backscatter data of a microfluidic tag with resonant frequency of 1 GHz. (d) Curve fit backscatter data of a microfluidic tag with resonant frequency of 900 MHz.

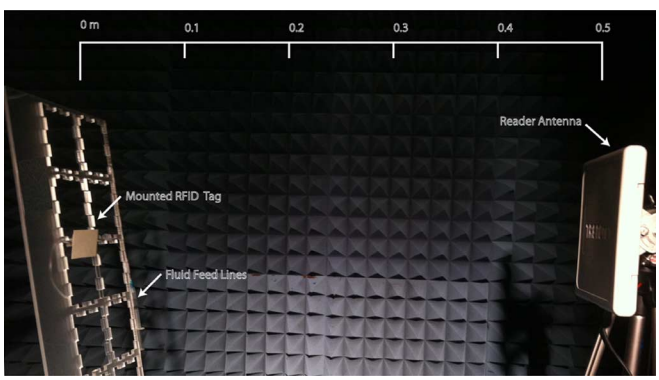

Fig. 12. Measurement setup of the wireless lab-on-chip RFID tag.

tag is emptied and again measured. The extracted resonant frequency of the empty tag is within a fraction of a percent of the empty measurement before being filled with an array of fluids. This demonstrates a high degree of repeatability which is important in long-term monitoring situations. It is noticed that the activation power slightly decreases with the higher permittivity fluids which is due to the improving matching between the antenna and chip impedance. The T-match is designed so that optimal matching occurs when the antenna resonant frequency is 900 MHz. It is seen from Fig. 11(b) that the wireless tag exhibits lower shifts than the cabled measurement, and this is due to the variation in chip impedance over frequency which is not taken into account in the simulation or cabled measurement. The variation in chip impedance along with the T-match cause a decreased sensitivity.

To test the effects of the chip impedance versus frequency on the sensitivity of the wireless LOC, a second version of the tag is fabricated in which the center frequency of tag antenna is tuned to 900 MHz by slightly increasing the length of the antenna. The Higgs 3 RFID chip typically has its own internal resonance around 900 MHz as well, which will overshadow some of the effects of the change in the electrical length of the antenna. By repeating the same procedure for wireless measurements with the previous tag, the curve-fit data of backscatter versus fluid flow is shown in Fig. 11(d). The resulting sensitivity is even lower than previous tag as the chip resonance begins to overshadow the electrical length change of the antenna.

VII. Conclusion

Utilizing a novel low-cost inkjet fabrication technique, varactors, tunable resonators, and completely passive wireless LOC systems have been demonstrated. The microfluidic sensing platform shows highly repeatable results with sensitivities that are sufficiently high to detect as little as 1% water in ethanol while using under 3 μL of fluid. The low-cost platform has applications in LOC, bio-monitoring, and real-time water and chemical analysis and monitoring.

REFERENCES

[1] A. W. Martinez, S. T. Phillips, B. J. Wiley, M. Gupta, and G. M. Whitesides, "Flash: A rapid method for prototyping paper-based microfluidic devices," *Lab on a Chip*, vol. 8, pp. 2146–2150, 2008.

[2] H. Klank, J. P. Kutter, and O. Geschke, "Co_2-laser micromachining and back-end processing for rapid production of PMMA-based microfluidic systems," *Lab on a Chip*, vol. 2, pp. 242–246, 2002.

[3] P. K. Yuen and V. N. Goral, "Low-cost rapid prototyping of flexible microfluidic devices using a desktop digital craft cutter," *Lab on a Chip*, vol. 10, pp. 384–387, 2010.

[4] B. S. Cook and A. Shamim, "Inkjet printing of novel wideband and high gain antennas on low-cost paper substrate," *IEEE Trans. Antennas Propag.*, vol. 60, no. 9, pp. 4148–4156, Sep. 2012.

[5] B. S. Cook, J. R. Cooper, and M. M. Tentzeris, "Multi-layer RF capacitors on flexible substrates utilizing inkjet printed dielectric polymers," *IEEE Microw. Compon. Lett.*, vol. 23, pp. 353–355, 2013.

[6] T. Le, V. Lakafosis, Z. Lin, C. P. Wong, and M. M. Tentzeris, "Inkjet-printed graphene-based wireless gas sensor modules," in *Procs. IEEE 62nd ECTC Conf.*, 2012, pp. 1003–1008.

[7] L. Yang, A. Rida, and M. M. Tentzeris, "Design and development of radio frequency identification (RFID) and RFID-enabled sensors on flexible low cost substrates," *Synthesis Lectures RF/Microw.*, vol. 1, pp. 1–89, 2009.

[8] L. Yang, A. Rida, R. Vyas, and M. M. Tentzeris, "RFID tag and RF structures on a paper substrate using inkjet-printing technology," *IEEE Trans. Microw. Theory Techn.*, vol. 55, no. 12, pp. 2894–2901, Dec. 2007.

[9] B. S. Cook, J. R. Cooper, S. Kim, and M. M. Tentzeris, "A novel inkjet-printed passive microfluidic RFID-based sensing platform," in *IEEE MTT-S Int. Microw. Symp. Dig.*, 2013, to be published.

[10] K. Shibata, "Measurement of complex permittivity for liquid materials using the open-ended cut-off waveguide reflection method," in *Proc. Microw. Conf.*, 2011, pp. 1–4.

[11] A. Tidar, S. Shafiyoddin, S. Kamble, G. Dharne, S. S. Patil, P. W. Khirade, 3, and S. C. Mehrotra, "Microwave dielectric relaxation study of 1-hexanol with j-propenol mixture by using time domain reflectometry at 300 K," in *Proc. Appl. Electromagn. Conf.*, 2009, pp. 1–4.

[12] N. Wiwatcharagoses, K. Y. Park, and J. Hejase, "Microwave artificially structured periodic media microfluidic sensor," in *Proc. IEEE Electron. Compon. Technol. Conf.*, 2011, pp. 1889–1893.

[13] N. Orloff, M. Rinehart, and J. Booth, "Broadband permittivity of liquids extracted from transmission line measurements of microfluidic channels," in *IEEE MTT-S Int. Microw. Symp. Dig.*, 2007, pp. 523–526.

[14] K. Grenier, D. Dubuc, P. Poleni, M. TKumemura, H. Toshiyoshi, T. Fujii, and H. Fujita, "New broadband and contact less RF/microfluidic sensor dedicated to bioengineering," *IEEE Trans. Microw. Theory Techn.*, vol. 57, pp. 1329–1332, 2009.

[15] S. Pavuluri, R. Lopez-Villarroya, E. McKeever, G. Goussetis, M. Desmulliez, and D. Kavanagh, "Integrated microfluidic capillary in a waveguide resonator for chemical and biomedical sensing," in *J. Phys.: Conf. Series*, 2009, vol. 178, pp. 1–6.

[16] K. Grenier, D. Dubuc, P.-E. Poleni, M. Kumemura, H. Toshiyoshi, T. Fujii, and H. Fujita, "Integrated broadband microwave and microfluidic sensor dedicated to bioengineering," *IEEE Trans. Microw. Theory Techn.*, vol. 57, no. 12, pp. 3246–3253, Dec. 2009.

[17] T. Chretiennot, D. Dubuc, and K. Grenier, "A microwave and microfluidic planar resonator for efficient and accurate complex permittivity characterization of aqueous solutions," *IEEE Trans. Microw. Theory Techn.*, vol. 61, no. 2, pp. 972–978, Feb. 2013.

[18] M. Hofmann, G. Fischer, R. Weigel, and D. Kissinger, "Microwave-based noninvasive concentration measurements for biomedical applications," *IEEE Trans. Microw. Theory Techn.*, vol. 61, no. 5, pp. 2195–2204, May 2013.

[19] B. Laemmle, K. Schmalz, J. Scheytt, R. Weigel, and D. Kissinger, "A 125-Ghz permittivity sensor with read-out circuit in a 250-nm SiGe BiCMOS technology," *IEEE Trans. Microw. Theory Techn.*, vol. 61, no. 5, pp. 2185–2194, May 2013.

[20] V. Sekar, W. Torke, S. Palermo, and K. Entesari, "A self-sustained microwave system for dielectric-constant measurement of lossy organic liquids," *IEEE Trans. Microw. Theory Techn.*, vol. 60, no. 5, pp. 1444–1455, May 2012.

[21] J. A. Gordon, C. L. Holloway, J. C. Booth, J. R. Baker-Jarvis, D. R. Novotny, S. Kim, and Y. Wang, "Fluid interactions with metafilm/metasurfaces for tuning, sensing, and microwave assisted chemical processes," *Phys. Rev. B*, vol. B83, 2011, Art. ID 205130.

[22] B. S. Cook, Y. Fang, S. Kim, T. Le, W. B. Goodwin, K. H. Sandhage, and M. M. Tentzeris, "Inkjet catalyst printing and electroless copper deposition for low-cost patterned microwave passive devices on paper," *Electron. Mater. Lett.*, vol. 9, no. 5, pp. 669–676, Sep. 2013.

[23] Microchem, "Su-8 2000," Tech. Rep. [Online]. Available: www.microchem.com

[24] J. Obrzut, A. Anopchenko, K. Kano, and H. Wang, "High frequency loss mechanism in polymers filled with dielectric modifiers," in *Proc. Mater. Res. Soc. Symp.*, 2004, vol. 783, pp. B3.5.1–B3.5.6.

[25] A. Sihvola, "Mixing rules with complex dielectric coefficients," *Subsurface Sensing Technol. Applic.*, vol. 1, pp. 393–415, 2000.

[26] T. Chen, D. Dubuc, M. Poupot, J. Fournie, and K. Grenier, "Accurate nanoliter liquid characterization up to 40 GHz for biomedical applications: Toward noninvasive living cells monitoring," *IEEE Trans. Microw. Theory Techn.*, vol. 60, no. 12, pp. 4171–4177, Dec. 2012.

[27] K. Grenier, D. Dubuc, T. Chen, F. Artis, T. Chretiennot, M. Poupot, and J. Fournie, "Recent advances in microwave-based dielectric spectroscopy at the cellular level for cancer investigations," *IEEE Trans. Microw. Theory Techn.*, vol. 61, no. 5, pp. 2023–2030, May 2013.

[28] K. P. Latti, M. Kettunen, J. P. Stoem, and P. Silventoinen, "A review of microstrip T-resonator method in determining the dielectric properties of printed circuit board materials," *IEEE Trans. Instrum. Meas.*, vol. 56, no. 5, pp. 1845–1850, Oct. 2007.

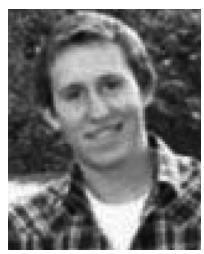

Benjamin S. Cook (S'12) received the B.Sc. degree in electrical engineering from Rose-Hulman Institute of Technology, Terre Haute, IN, USA, in 2010, and the M.A.Sc. degree in electrical engineering from King Abdullah University of Science and Technology, Thuwal, Saudi Arabia, in 2011. He is currently working toward the Ph.D. degree in electrical engineering at Georgia Institute of Technology, Atlanta, GA, USA.

He has authored and coauthored over 25 peer-reviewed publications. His research focuses are in inkjet process design for vertically integrated millimeter-wave devices, system-on-paper applications, green electronics, MEMS device fabrication, RF energy harvesting, and passive wireless sensors.

Mr. Cook was the recipient of the Outstanding Senior Electrical and Computer Engineering Student of the Year Award at Rose-Hulman Institute of Technology, the King Abdullah University of Science and Technology (KAUST) Fellowship Award in 2010, and the KAUST Provost Award in 2011. During the course of his Ph.D. work, he has received the IEEE Antennas and Propagation Society Doctoral Research Award and the Intel Doctoral Fellowship for his work in vertically integrated inkjet fabrication for millimeter-wave applications.

James R. Cooper (S'13) received the B.S. and M.S. degree in electrical engineering from the University of South Florida, Tampa, FL, USA, in 2008 and 2010, respectively. He is currently working toward the Ph.D. degree in electrical and computer engineering at the Georgia Institute of Technology, Atlanta, GA, USA.

He is currently performing research with the ATHENA Research Group under Dr. Manos Tentzeris. His research is in the area of passive and wireless circuit and device design in the microwave and millimeter-wave range. He also performs research in the area of novel material design for inkjet printing.

Mr. Cooper was the recipient of the Award for Outstanding Research from the College of Engineering at USF, NSF GK12 Students, Teachers and Resources in Science (STARS) Fellowship from the College of Engineering at USF, and the Graduate Research Fellowship Program (GRFP) Fellowship from NSF.

Manos M. Tentzeris (S'89–M'92–SM'03–F'10) received the Diploma Degree in electrical and computer engineering (*magna cum laude*) from the National Technical University of Athens, Athens, Greece, and the M.S. and Ph.D. degrees in electrical engineering and computer science from the University of Michigan, Ann Arbor, MI, USA.

He is currently a Professor with the School of Electrical and Computer Engineering, Georgia Institute of Technology (Georgia Tech), Atlanta, GA, USA. He has authored and coauthored more than 420 papers in refereed journals and conference proceedings, five books, and 19 book chapters. He has helped develop academic programs in Highly Integrated/Multilayer Packaging for RF and Wireless Applications using ceramic and organic flexible materials, paper-based RFIDs and sensors, biosensors, wearable electronics, inkjet-printed electronics, "green" electronics and power scavenging, nanotechnology applications in RF, microwave MEMS, SOP-integrated (UWB, multiband, millimeter-wave, conformal) antennas and adaptive numerical electromagnetics (FDTD, multiresolution algorithms) and heads the ATHENA Research Group (20 researchers). He is currently the Head of the GT-ECE Electromagnetics Technical Interest Group and has served as the Georgia Electronic Design Center Associate Director for RFID/Sensors research from 2006 to 2010 and as the Georgia Tech NSF-Packaging Research Center Associate Director for RF Research and the RF Alliance Leader from 2003 to 2006.